International Journal of Heat and Mass Transfer 88 (2015) 261–275

Contents lists available at ScienceDirect

International Journal of Heat and Mass Transfer

journal homepage: www.elsevier.com/locate/ijhmt

Condensation heat transfer of R245fa in tubes with and without lyophilic porous-membrane-tube insert

Jian Xie, Jinliang Xu *, Yu Cheng, Feng Xing, Xiaotian He

The Beijing Key Laboratory of Multiphase Flow and Heat Transfer, North China Electric Power University, Beijing 102206, China

ARTICLE INFO

Article history:
Received 8 December 2014
Received in revised form 23 April 2015
Accepted 24 April 2015

Keywords:
Modulated heat transfer tube
Porous membrane tube
Condensation heat transfer
Flow pattern
Organic Rankine cycle

ABSTRACT

Modulated heat transfer tube (MHTT) is called by suspending porous-membrane-tube (PMT) in a large tube to form an annular region and a core region. PMT was made by sintering copper powders in a circular membrane shape, which is lyophilic to capture liquid and make liquid flowing towards PMT inside. Vapor phase is prevented from entering PMT. Thus, vapor void fractions near the tube wall are increased to enhance condensation heat transfer. Experiments were performed with a copper tube inner diameter of 14.81 mm and a heat transfer length of 1200 mm. R245fa was the working fluid. Great attention was paid to explain condensation heat transfer coefficients influenced by mass fluxes, vapor mass qualities and inclination angles. It was found that MHTT had 85% improvement of condensation heat transfer coefficients compared with bare tube (BT), maximally. The heat transfer enhancement factors of MHTT were increased with mass fluxes and/or vapor mass qualities. MHTT had largest condensation heat transfer coefficients for the vertical upflow, due to the promoted liquid mass and momentum exchange across the porous membrane. MHTT had smallest condensation heat transfer coefficients for the horizontal flow. The droplet capture and liquid flow to PMT are the heat transfer enhancement mechanism for annular flow modulation. Alternatively, the capillary pumping effect held liquid within PMT to decrease liquid height in the annular region, accounting for the heat transfer enhancement mechanism for stratified flow modulation. This paper finds a new clue to use PMT in a large tube for phase change heat transfer enhancement.

1. Introduction

There are huge waste heat resources in various industry sectors. Recovery of waste heat (for example, flue gas heat) is important to save energy and decrease environment pollution. A diesel engine only converts about 40% of the fuel combustion energy to useful power, leaving more than half of the fuel combustion energy released to environment with flue gas as the heat carrier fluid [1]. For a coal fired power plant, the flue gas carries about 10% of the coal combustion energy which is discharged to environment [2]. Usually, waste heat belongs to the low grade energy since it is usually available at a temperature close to ambient temperature. The low grade energy also includes renewable energy such as solar energy, geothermal energy, etc. Conventionally, low grade energy can drive refrigeration or heat pump systems [3,4]. Alternatively, organic Rankine cycles (ORCs) convert low grade thermal energy to power or electricity. Electricity belongs to high grade energy, which is convenient for users. ORC is still in the infancy stage with many technical issues that should be addressed before it is used commercially [5]. Selection of organic fluids, expanders, evaporators and condensers are paid great attention [6].

Organic fluids, such as R245fa, can evaporate at relatively low temperature, as compared with water. The vapor has considerable pressure to drive expander for power generation. Most of organic fluids can receive heat at the temperature of 100 °C to produce vapor pressure up to ~1 MPa, which is impossible for water-vapor Rankine cycle. For water, the vapor pressure is only 1.013 bar at the temperature of 100 °C. The low water-vapor pressure is not useful for power generation.

Organic fluids have physical properties significantly different from water. Recently, R245fa is widely recommended for ORCs [7–9]. For R245fa, the surface tension force is 25% and latent heat of evaporation is 9% of those for water at atmospheric pressure.

In fact, organic fluids have been widely applied in air-conditionings. Capillary tubes have inside diameter of about 8 mm. Microstructures on tube wall enhance phase change heat transfer. Micro groove tubes [10], micro-fin tubes [11], herringbone tubes [12] and helically corrugated tubes [13] are the enhanced condensation tubes. The heat transfer enhancement

* Corresponding author. Tel.: +86 10 61772613.
E-mail address: xjl@ncepu.edu.cn (J. Xu).

http://dx.doi.org/10.1016/j.ijheatmasstransfer.2015.04.081
0017-9310/

Nomenclature

A	annular flow
AC	alternative current
BT	bare tube
Bd	Bond number
C	churn flow
C_p	specific heat at constant pressure, J/(kg K)
D or d	diameter, m
e	deviation
e_R	average deviation
e_A	average absolute deviation
EF	heat transfer enhancement ratio
F	falling film flow
Fr	Froude numbers
g	acceleration of gravity, m/s^2
G	mass flux, kg/(m^2 s)
h or h'	heat transfer coefficient, W/(m^2 K)
H_l	the liquid height, m
i	enthalpy, J/kg
i_{fg}	latent heat of evaporation, J/kg
I	current, A
I	intermittent flow
k	thermal conductivity, W/(m K)
$\tilde{k}$	rate of circumference length exposed in the vapor phase
L	length, m
L_{ue}	length between focus point of upstream to exit of porous-membrane-tube, m
$LMTD$	logarithmic mean temperature difference, °C or K
m	mass flow rate, kg/s
MHTT	modulated heat transfer tube
n	total number of cross sections divided along the flow direction
ORC	organic Rankine cycle
P	pressure, Pa
PEC	performance evaluation parameter
ΔP_f	frictional pressure drop, Pa
PMT	porous-membrane-tube
q	heat flux on the inner wall surface, W/m^2
Q	heat transfer rate or heat transfer rate per unit flow length, W or W/m
r	radius of the wetting area, m
R	thermal resistance, K/W
S_v	circumference length exposed in the vapor phase, m
SEM	scanning electron microscope
SW	stratified wavy flow
t	time, s
T	temperature, °C or K
ΔT	temperature difference between the vapor and tube wall, °C or K
ΔT_c	temperature rise of the cooling water in the tube annulus, °C or K
U	voltage, V
u_r	spreading velocity in redial direction, m/s
w	pore width of porous-membrane-tube, m
We	Weber number
x	vapor mass quality
$\tilde{x}_1, \tilde{x}_2, \tilde{x}_3 \ldots \tilde{x}_n$	independent variables
$\Delta\tilde{x}_1, \Delta\tilde{x}_2, \Delta\tilde{x}_3 \ldots \Delta\tilde{x}_n$	uncertainties of independent parameters
Y	any dependent variable
ΔY	uncertainties of the dependent parameter
z	axial coordinate, m

Greek symbols

α_h	thin film condensation heat transfer coefficient
δ	thickness of porous-membrane-tube, m
θ	inclination angle, °
η	thermal efficiency
ρ	density, kg/m^3
ρ_m	two-phase mixture density in the annular region
σ	surface tension, N/m
σ_n	standard deviation
Φ	diameter of the wetting area, m
ϕ_{lo}^2	two-phase flow multiplier

Subscript

1	evaporator inlet
2	evaporator outlet
A	cross section A–A (see Fig. 15)
an	annular region
ave	average
b	bottom wall location
B	cross section B–B (see Fig. 15)
BT	bare tube
c	cooling water
co	core region
con	condenser
e	exit
eff	effective heat transfer
eva	evaporator
exp	experiment
f	liquid
g	vapor
gl	glass
h	heat transfer
i	inside wall surface
in	condenser inlet
ins	inside wall surface of shell tube
j	the cross section number along the flow direction
l	liquid
MHTT	modulated heat transfer tube
o	outer wall surface
out	condenser outlet
p	porous-membrane-tube
pre	prediction
r	organic fluid (R245fa in this study)
s	side wall location
t	top wall location
to	total
u	upstream
w	wall

mechanism is attributed by mixing the fluid boundary layers and limiting the growth of fluid boundary layers close to the wall surfaces.

Lips and Meyer [14] investigated convective condensation of R134a in an 8.38 mm inner diameter smooth tube. Results for the whole range of inclination angles were presented. The flow pattern is dependent on the inclination angle for low mass fluxes and/or low vapor qualities. There is an optimum inclination angle that leads to the highest heat transfer coefficient for downward flow. The heat transfer coefficient is strongly affected by the liquid and vapor distributions and especially by the liquid thickness at the bottom of the tube for stratified flows. Cavallini et al. [15] investigated condensation heat transfer and pressure losses of high- and low-pressure refrigerants flowing in a single circular

minichannel. The heat transfer experimental data are compared against predicting models to provide a guideline for design of minichannel condensers.

The situation is changed when these techniques are applied for ORCs. Usually, heat received from the low grade energy source is in 1−10 MW scale for ORCs, which is several orders larger than that for air-conditionings. The condenser tube had apparently larger diameter than 8 mm. Issues related to the phase change heat transfer of organic fluids are as follows. First, organic fluids have low specific heat and latent heat of evaporation, yielding poor phase change heat transfer than that for water. When the heat transfer enhancement techniques used in air-conditionings are extended for ORCs, these techniques should be re-investigated. Second, the combination of low surface tension force and larger tube diameter influenced the phase distribution to affect heat transfer. Gupta et al. [16] commented on the non-dimensional parameters in two-phase systems as Reynolds number, Froude number, Bond number, capillary number, and Weber number. Gravity force is involved in Froude number and Bond number. The tube diameter is involved in all the dimensionless parameters except capillary number. Both gravity force and inertia force are important to influence flow patterns and heat transfer. The combination of low surface tension force and larger tube diameter yields larger Bond number and Weber number to make unstable vapor-liquid interface.

Recently, our group [17,18] proposed the phase separation concept to modify flow patterns. An empty mesh-screen-membrane was suspended in the tube. Mesh pores prevented gas bubbles from entering the mesh cylinder but captured liquid into the mesh cylinder, increasing gas void fractions near the tube wall. An adiabatic air-water two-phase flow experiment was performed to verify the idea. The bubbly, slug and plug flows were successfully modulated. Subsequently, we performed the numerical simulation of flow pattern modulations for air-water vertical upflows [19]. The results did show zero void fractions inside the mesh cylinder and higher gas void fractions near the tube wall. Liquid film thicknesses in the modulated flow section were 1/6–1/3 of those in the bare tube section.

Here we report condensation heat transfer data with the phase separation concept. The membrane tube was made by sintering copper powders at high temperature to form circular membrane. The R245fa vapor-liquid mixture existed at the condenser tube inlet. R245fa fluid is low toxicity and non-flammability. The copper tube had an inner diameter of 14.81 mm and an outer diameter of 18.97 mm. Such tube can be used in condensers of ORCs [20].

This paper was organized as follows. Section 2 described experimental details, including experimental loop, test section, data reduction and uncertainty, degassing of the R245fa fluid and calibration experiment. Section 3 reported results and discussion. Section 3.1 reported measured condensation heat transfer coefficients with and without the porous-membrane-tube (PMT) insert. Section 3.2 described observed flow patterns in the bare tube. Section 3.3 gave a general explanation of the enhanced heat transfer. Section 3.4 dealt with enhanced heat transfer mechanisms for specific flow patterns. The main conclusions were summarized in Section 4.

2. Experimental setup, materials and methods

2.1. Experimental loop

The experimental setup consisted of an organic fluid loop, an evaporator section, a test section, a chiller water loop, a tap water cooled post-condenser and relevant instruments (see Fig. 1). The R245fa fluid was circulated by the organic fluid loop. Initially, non-condensable gas was vacuumed from the loop by a vacuum pump and then the loop was charged by R245fa liquid from a reservoir. A diaphragm pump provided R245fa flow rate to the loop, ensuring no lubrication oil in the R245fa fluid. A specific pump flow rate was obtained by setting pump frequency and diaphragm displacement. Fluid pressure was stabilized by an accumulator at the pump outlet, having a specific liquid level pressurized by nitrogen gas. The R245fa liquid and nitrogen gas were separated by a piece of flexible membrane so that non-condensable gas cannot enter R245fa liquid.

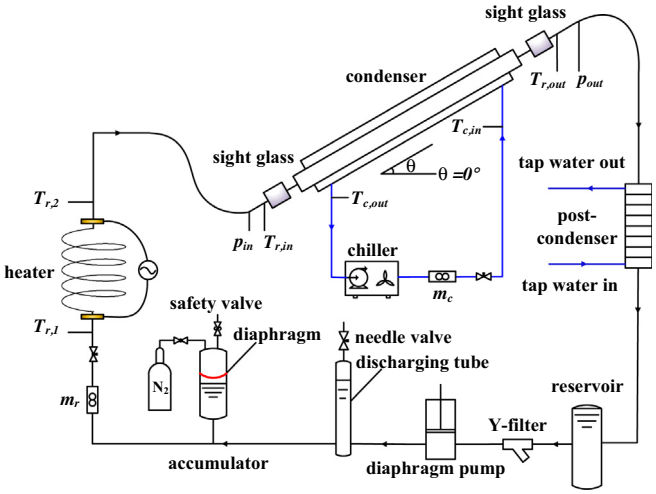

Fig. 1. The experimental setup.

A helical-coiled tube was heated by an AC (alternative current) electrical power to be the evaporating section. A transformer converted high voltage (380 V) AC to low voltage AC. Two copper plates were welded on the curved tube and acted as electrodes. The evaporating section was electrically insulated with other components of the loop. A thick thermal insulation material was wrapped on the curved tube. The power was obtained by the measured voltage and current. The evaporating section inlet was subcooled liquid with a temperature of $T_{r,1}$. $T_{r,2}$ was the outlet temperature. The evaporator outlet had a saturation temperature ($T_{r,2}$). A bare tube (called BT without any insert) and a modulated heat transfer tube (called MHTT with porous-membrane-tube PMT insert) were tested, respectively. The test section was tightly positioned on an angle adjustment facility. Thus, it can be rotated at any inclination angles with an uncertainty of 0.5°.

A chiller water loop condensed the two-phase mixture in the test section. The water loop included a chiller, a mass flow meter and two sheathed thermocouples. A stable chiller water flow rate, m_c, was measured by a mass flow meter. The heat was dissipated by a fan to ambient air. Two thermocouples ($T_{c,in}$ and $T_{c,out}$) measured the inlet and outlet temperatures of the chiller water. The two-phase R245fa mixture was further condensed by a post-condenser to subcooled liquid. The tap water flow rate was regulated by a regulating valve precisely.

2.2. Test section

Fig. 2 shows the counter-current condenser test section, consisting of two sight glass tube adaptors, a copper tube and an outer stainless steel tube. Two flanges connected the sight glass tube to the copper tube. The effective condensation length was 1200 mm. Based on Cao et al. [21], if a long porous-membrane-tube was suspending in a tube, liquids maybe over-sucked into the membrane tube to weaken the effectiveness of the modulated heat transfer tube. Thus, four short porous-membrane-tubes were suspending

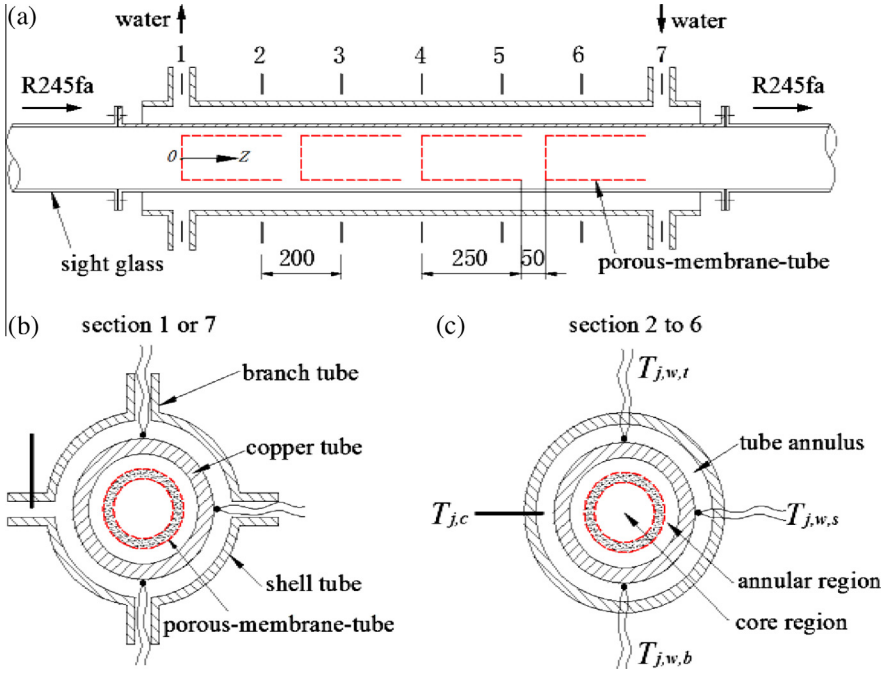

Fig. 2. The modulated condensation heat transfer tube.

in the copper tube and they were arranged consecutively along the flow direction. Each of the membrane tube had a length of 250 mm, with an axial distance of 50 mm between two neighboring porous-membrane-tubes (see Fig. 2a).

Along the flow length of 1200 mm, seven cross sections were marked as 1−7. The distance between two neighboring cross sections was 200 mm (see Fig. 2a). The cross sections 1 and 7 were for the R245fa fluid inlet and outlet, respectively (see Fig. 2b). Four branch tubes were welded to the outer stainless steel tube to vent the cooling water from the tube annulus. Three thermocouple wires were tightly buried under a thin copper film on the top, side and bottom wall locations. The thermocouple wires penetrated the shell tube for signal processing. A sheathed thermocouple near the junction of the branch tube and the shell tube measured the cooling water temperature. The cross sections 2–6 did not contain the branch tube. The three thermocouples on the tube wall were marked as $T_{j,w,t}$, $T_{j,w,s}$ and $T_{j,w,b}$, where j refers to the cross section number (j = 2–6), w refers to the wall, t, s and b refers to the top, side and bottom locations, respectively. $T_{j,c}$ measured the cooling water temperature in the tube annulus with c standing for the cooling water. The porous-membrane-tube divided the copper tube into a core region and an annular region (see Fig. 2c). The cooling water flowed in the tube annulus. The shell tube had an inner diameter of 23.80 mm with a tube annulus of 2.41 mm. The BT was exactly the same as the MHTT, except that it did not contain PMT insert.

Fig. 3a shows thermocouple arrangement on the copper tube wall. Initially, a hammer hit the point chisel on the copper tube wall to lift a thin copper film from the tube wall. The thermocouple wire was buried in the cavity beneath the copper film. Finally, the hammer hit the blunt chisel on the copper film to tightly populate the thermocouple wire in the cavity.

Once all the thermocouple wires were arranged on the tube wall, the twenty-one thermocouples (three for each cross section, seven cross sections) were pulled simultaneously to penetrate the corresponding holes on the shell tube (see Fig. 3b). The process was over until the buried locations of thermocouple wires were at the same cross section as the corresponding holes were. Such process ensured shortest thermocouple wire length exposed in the tube annulus. The thermocouple wires were slim with a diameter of 0.30 mm. The outer surface of thermocouple wires was thermally insulated by coating a thin layer of teflon film with the thermal conductivity of 0.25 W/m K. The disturbance of thermocouple wires on flow field in the tube annulus was minimized and the thermal conductivity effect of thermocouple wires was negligible.

Fig. 3c shows how the PMT was inserted in the copper tube. Four PMTs were connected with each other by welding themselves to copper wires. Each copper wire was carefully chosen to have a diameter equivalent to the annular gap size. It had a length slightly longer than the distance between two neighboring PMTs. Two grooves were fabricated on the copper tube over the entrance cross section. The groove width was the same as the copper wire diameter. The two copper wires for the first PMT section were buried in the grooves of the copper tube.

Fig. 4 shows the packaged MHTT. The outer shell tube was not shown. The copper tube had an outer diameter of D_o = 18.97 mm with a thickness of 2.08 mm. It had an inner diameter of D_i = 14.81 mm, with a heat transfer length of L_{eff} = 1200 mm. Fig. 4b shows the PMT photo, which was made by sintering copper powders at high temperature. The copper powder had an average diameter of 170 μm. The porous tube had a flat and "closed" side porous plane, but it had an open exit to discharge the collected liquid. The SEM (scanning electron microscope) image shows that the pore sizes were in the range of 20−30 μm. The PMT had an outer diameter of d_o = 10.70 mm and an inner diameter of d_i = 8.00 mm. The thickness of the porous membrane δ was 1.35 mm. Table 1 summarized the material and size of various components of the test section.

For phase change heat transfer, it is important to remove non-condensable gas from liquid. Following measures were taken: (1) non-condensable gas was vacuumed from the experimental loop before charging R245fa liquid; (2) the R245fa liquid was separated from nitrogen gas by a flexible diaphragm in the liquid accumulator; (3) a long non-condensable gas discharging tube was positioned vertically at the pump outlet (see Fig. 1). Before

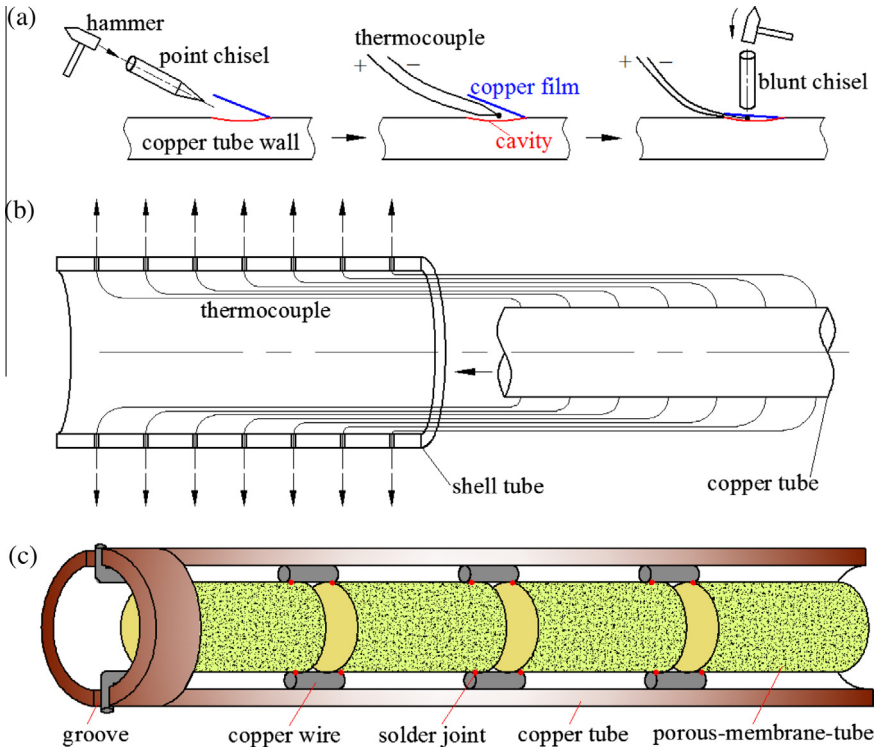

Fig. 3. Thermocouples buried in the copper tube cavity (a), thermocouple wires penetrated the copper tube wall to the shell tube outside (b) and PMT installation in the copper tube (c).

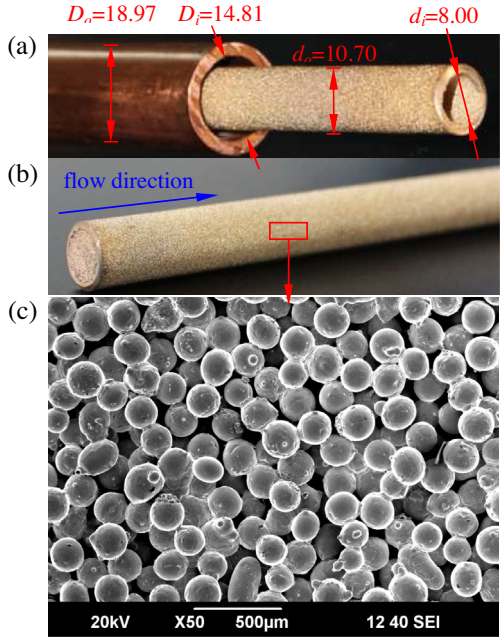

Fig. 4. The porous-membrane-tube inserted in the copper tube.

formal experiment, convective flow was established. The voltage heating was applied to R245 liquid by the helical coiled tube. Non-condensable gas was released from liquid due to heating. The released gas was accumulated in the discharging tube. After a couple of hours' operation, the safety valve at the top of the discharging tube was manually opened to discharge gas to environment. Continuous operation of the loop yielded no-any gas emission but the valve discharged pure liquid only. It is assured that non-condensable gas was thoroughly removed.

2.3. Data reduction and uncertainty analysis

2.3.1. Inlet and outlet vapor mass qualities (x_{in} and x_{out})

The condenser inlet enthalpy, $i_{r,in}$, and quality, x_{in}, were based on the measured parameters in the evaporator and the calibrated evaporator efficiency, η_{eva}:

$$i_{r,in} = i_{r,1} + \frac{UI\eta_{eva}}{m_r} \tag{1}$$

$$x_{in} = \frac{i_{r,in} - i_{l,in}}{i_{fg,in}} \tag{2}$$

where $i_{r,1}$ is the R245fa enthalpy at the evaporator inlet, $i_{l,in}$ is the R245fa saturated liquid enthalpy, i_{fg} is the latent heat of evaporation, U and I are voltage and current, respectively. The determination of η_{eva} can be seen in Section 2.4.

Similarly, the condenser efficiency (η_{con} in Section 2.4) was used to compute the condenser outlet parameters. Heat received by the cooling water in the tube annulus was

$$Q = m_c C_{p,c}(T_{c,out} - T_{c,in}) = m_c C_{p,c}\Delta T_c \tag{3}$$

Table 1
The major parameters of components for the test section.

Components	Materials	Parameters
Shell tube	304SS	D_{ins} = 23.80 mm
Copper tube	Copper	D_i = 14.81 mm, D_o = 18.97 mm, L_{eff} = 1200 mm
PMT	Brass	d_o = 10.70 mm, d_i = 8.00 mm, δ = 1.35 mm, L_p = 250 mm, d_p = 170 μm, w = 20–30 μm
Sight glass	Quartz	D_{gl} = 15.80 mm, L = 200 mm

where ΔT_c is the cooling water temperature difference between outlet and inlet. Heat flux based on the inner copper tube wall was

$$q = \eta_{con} Q/(\pi D_i L_{eff}) \tag{4}$$

where L_{eff} is the effective heat transfer length (L_{eff} = 1.20 m), D_i = 14.81 mm. The outlet two-phase mixture enthalpy and vapor mass quality were

$$i_{r,out} = i_{r,in} - Q\eta_{con}/m_r \tag{5}$$

$$x_{out} = \frac{i_{r,out} - i_{l,out}}{i_{fg,out}} \tag{6}$$

where $i_{l,out}$ and $i_{fg,out}$ are the saturated liquid enthalpy and latent heat of evaporation based on the outlet pressure, respectively.

2.3.2. Heat transfer coefficient

The total condenser thermal resistance included condensation thermal resistance, R_r, thermal conduction thermal resistance, R_w, and cooling water resistance in the tube annulus, R_c:

$$R_{to} = R_r + R_w + R_c \tag{7}$$

$$R_{to} = \frac{1}{\pi D_i L_{eff} h_{to}},\quad R_r = \frac{1}{\pi D_i L_{eff} h},\quad R_w = \frac{\ln(D_o/D_i)}{2\pi L_{eff} k_w},\quad R_c = \frac{1}{\pi D_o L_{eff} h_c} \tag{8}$$

where h_{to}, h, h_c are the heat transfer coefficients of total, condensation, and cooling water, respectively, D_i and D_o are the inner and outer diameters of the copper tube. Thus, h was

$$h = \frac{1}{\frac{1}{h_{to}} - \frac{D_i}{2k_w}\ln\left(\frac{D_o}{D_i}\right) - \frac{D_i}{D_o}\frac{1}{h_c}} \tag{9}$$

The total heat transfer coefficient h_{to} in Eq. (9) was

$$h_{to} = \frac{q}{LMTD} \tag{10}$$

In which q was predicted by Eqs. (3) and (4), the $LMTD$ temperature difference was

$$LMTD = \frac{(T_{r,in} - T_{c,out}) - (T_{r,out} - T_{c,in})}{\ln\left(\frac{T_{r,in} - T_{c,out}}{T_{r,out} - T_{c,in}}\right)} \tag{11}$$

$$h_c = \frac{qD_i}{D_o(T_{w,ave} - T_{c,ave})} \tag{12}$$

where the subscripts r and c represent R245fa fluid and cooling water, respectively, $T_{w,ave}$ and $T_{c,ave}$ are the average temperatures of the tube wall and the cooling water, which are

$$T_{w,ave} = \frac{1}{3n}\sum_{j=1}^{n} T_{j,w,t} + T_{j,w,s} + T_{j,w,b},\quad T_{c,ave} = \frac{1}{n}\sum_{j=1}^{n} T_{j,c} \tag{13}$$

The subscripts t, s and b refer to the top, side and bottom wall (see Fig. 2c), j is the cross section number, n equals to 7 here.

2.3.3. Heat transfer enhancement ratio

Heat transfer enhancement ratio was defined as the condensation heat transfer coefficient for MHTT divided by that for BT at the same inclination angle, $EF = h_{MHTT}/h_{BT}$, noting that EF is a global parameter over the whole heat transfer length. Table 2 summarized the major parameter ranges.

2.3.4. Uncertainty analysis

High quality sensors and instruments were used. For instance, temperature and mass flow rate were measured by OMEGA K-type thermocouples and DMF-1-DX mass flow meter, respectively. Before formal experiment, standard calibration procedures were performed. Temperature and mass flow rate had uncertainties of 0.2 °C and 0.1%, respectively. Heat transfer coefficient and thermal resistance were determined by a set of measured parameters. Uncertainties of these parameters were evaluated based on the error transmission theory [22]. If Y is a given function of the independent variables of $\tilde{x}_1$, $\tilde{x}_2$, $\tilde{x}_3 \ldots \tilde{x}_n$ and $\Delta\tilde{x}_1$, $\Delta\tilde{x}_2$, $\Delta\tilde{x}_3 \ldots \Delta\tilde{x}_n$ are uncertainties of these independent parameters, the uncertainty of Y is

$$\Delta Y = \sqrt{\left(\frac{\partial Y}{\partial \tilde{x}_1}\Delta\tilde{x}_1\right)^2 + \left(\frac{\partial Y}{\partial \tilde{x}_2}\Delta\tilde{x}_2\right)^2 + \cdots \left(\frac{\partial Y}{\partial \tilde{x}_n}\Delta\tilde{x}_n\right)^2} \tag{14}$$

Finally, heat transfer coefficient and enhanced heat transfer ratio had uncertainties of 2.37–9.04% and 3.73–12.23%, respectively. Table 3 summarized uncertainties. The uncertainty of heat transfer coefficients was strongly dependent on temperature measurements. The uncertainty of h will be decreased to 1.31–4.97% if one uses temperature sensors with uncertainty of 0.1 °C.

Table 2
The data ranges of measured parameters.

Parameters	Ranges
Inclination angle (°)	−90, 0, 90
Mass flux of R245fa flow (kg/m^{2}s)	199.0–502.7
Inlet temperature of the helical-coiled tube (°C)	15.0 ± 0.4
Inlet pressure of the test section (kPa)	404.9 ± 3.0
Inlet temperature of the test section (°C)	55.4 ± 0.3
Inlet vapor mass quality of the test section	0.048–0.917
Mass flow rates of the cooling water (kg/h)	500.0 ± 3.0
Inlet temperature of the cooling water (°C)	25.0 ± 0.3
Heat flux on the inner wall surface (kW/m^2)	20.83–81.00

2.4. Calibration experiment

Because two-phase mixture enthalpy cannot be determined by its temperature alone, single-phase liquid heat transfer experiments were performed to obtain evaporator and condenser thermal efficiencies. The evaporator thermal efficiency with R245fa liquid was

$$\eta_{eva} = \frac{m_r C_{p,r}(T_{r,2} - T_{r,1})}{UI} \tag{15}$$

where m_r is the R245fa mass flow rate, $C_{p,r}$ is the specific heat of R245fa liquid, $T_{r,1}$ and $T_{r,2}$ are liquid temperatures at the evaporator inlet and outlet, respectively, U is the voltage and I is the current. The measured thermal efficiency was in the range of 0.95–0.99. Thus, the evaporator thermal efficiency was set as 0.97.

Then, condenser thermal efficiency (organic fluid side), η_{con}, was

$$\eta_{con} = \frac{m_c C_{p,c}(T_{c,out} - T_{c,in})}{m_r C_{p,r}(T_{r,in} - T_{r,out})} \tag{16}$$

where m_c is the cooling water mass flow rate, $C_{p,c}$ is the water specific heat, $T_{c,out}$ and $T_{c,in}$ are the outlet and inlet water temperatures,

Table 3
The major parameters, instruments and uncertainties.

Parameters	Instruments	Uncertainties
Wall temperature	K-type thermocouple wire	0.2 °C
Fluid temperature	K-type jacket thermocouple	0.2 °C
R245fa mass flow rate	DMF-1-DX mass flow meter	0.1%
Water mass flow rate	DMF-1-DX mass flow meter	0.1%
Pressure	Rosemount-3051 pressure transducer	1.0%
h		2.37–9.04%
EF		3.73–12.23%

respectively. The measured η_{con} reached about 0.98. The values of η_{eva} and η_{con} are used by Eqs. (1) and (4) in Section 2.3. Thermal efficiencies of evaporators and condensers were smaller than one, due to heat loss from tube wall to environment. The evaporator effectiveness was calibrated in single phase liquid region. Because during single phase operation, evaporator wall temperatures were kept as the same level as those during two-phase operation, the thermal efficiency can be extended to be used for two-phase region. Similar extension was made for the condenser thermal efficiency.

Friction factor and Nusselt number were measured for single-phase liquid flow in the bare tube. The measured friction factors in turbulent liquid flow regime agreed well with those computed by the Blasius expression [23], with the difference between them less than 8.07%. The measured Nusselt number also matched the Dittus–Boelter correlation [24] well, with the relative difference less than 6.39%.

In addition to the single-phase liquid heat transfer test, condensation heat transfer coefficient data in the bare tube was obtained and compared with the Shah correlation [25]. Fig. 5 included the data at the inclination angles of 0°, 90° and -90°. Various deviations were defined to evaluate experimental data compared with the Shah correlation.

$$e = \frac{h_{pre} - h_{\exp}}{h_{\exp}} \times 100\% \tag{17}$$

$$e_R = \frac{1}{n}\sum_{1}^{n}\left[\frac{h_{pre} - h_{\exp}}{h_{\exp}}\right] \times 100\% \tag{18}$$

$$e_A = \frac{1}{n}\sum_{1}^{n}\left[\frac{|h_{pre} - h_{\exp}|}{h_{\exp}}\right] \times 100\% \tag{19}$$

$$\sigma_n = \left\{\left[\sum_{1}^{n}(e - e_R)^2\right] \Big/ (n-1)\right\}^{1/2} \times 100\% \tag{20}$$

where e, e_R, e_A, σ_n are the sample deviation, average deviation, average absolute deviation and standard deviation, which were 6.79% for e_R, 8.22% for e_A and 8.88% for σ_n. Thus, our experimental loop and instrument are acceptable for the condensation heat transfer experiment.

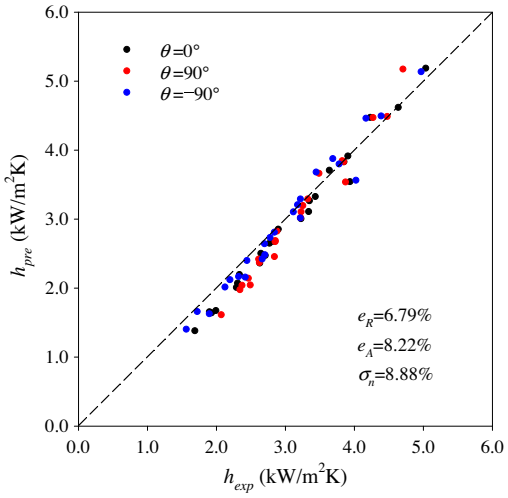

Fig. 5. Comparison between measured and predicted heat transfer coefficients with the Shah correlation [25].

2.5. Additional comment on our experiment

Table 4 shows part of the experimental runs (totally 92 runs were performed in this study). Negligible gas in R245fa liquid can be verified by examining measurements of vapor pressures and temperatures. For example, run 1 had the measured pressure of 402.1 kPa. The measured temperature was 55.1 °C, which approached the pressure determined saturation temperature of 55.2 °C.

PMT insert decreased cross sectional area to increase mass flux (G). Heat transfer enhancement was partially due to the increased G. Runs 53 and 54 (see Table 4) were the example cases. Run 53 had h = 3.122 kW/m^2 K with G = 400.4 kg/m^2 s. Run 54 would have G = 520.1 kg/m^2 s if the decreased cross section area was considered. For BT, the measurement was h = 3.931 kW/m^2 K with G = 520 kg/m^2 s, inferring 25.91% improved heat transfer. For MHTT, run 54 had h = 5.445 kW/m^2 K, showing 74.44% improved heat transfer compared with BT. Thus, the phase separation concept had 48.53% improved heat transfer. The phase separation concept had larger heat transfer enhancement factor than the decreased cross section area effect.

Table 4 lists vapor mass qualities at the inlet (x_{in}) and outlet (x_{out}) for each run. Because our experimental procedure can keep almost the same x_{in} for a comparative runs, heat transfer coefficients were plotted versus x_{in} only, noting that the vapor quality difference was x_{in}–x_{out} for each run.

Condensation heat transfer coefficient (h) was determined in Section 2.3. It can also be directly obtained from inside wall based hat flux and internal wall temperature (calculated from measured outer wall temperature considering thermal conduction in copper tube). The heat transfer coefficient was recorded as h' and the method was described in ref. [26]. Table 4 shows that the difference between h and h' is very small, with maximum deviation of 3.84% for the 56 runs.

It is important to report how much of the heat transfer enhancement is paid in terms of pressure drop increase. Table 4 lists the two-phase frictional pressure drop (ΔP_f) for each run, which was deduced from measured total pressure drop subtracting acceleration pressure drop and gravity pressure drop. The deduction method was described in Refs. [27,28]. An efficient way to evaluate heat transfer enhancement at the cost of pressure drop was the performance evaluation parameter (*PEC*), which was defined as

$$PEC = \frac{h_{\mathrm{MHTT}}/h_{\mathrm{BT}}}{\left(\Delta P_{f,\mathrm{MHTT}}/\Delta P_{f,\mathrm{BT}}\right)^{1/6}} \tag{21}$$

A heat transfer device is recommended for applications if *PEC* is larger than one [29,30]. Table 4 shows that most of runs had *PEC* larger than one.

The thermal conduction resistance of the tube wall was small. The dominant thermal resistance was on the refrigerant fluid side. For example, runs 1 and 17 had the thermal resistances on the refrigerant side of 9.41 K/kW and 5.36 K/kW, respectively. But the two runs had the thermal resistances on the cooling water side of 2.41 K/kW and 2.32 K/kW, respectively.

3. Results and discussion

3.1. Enhanced heat transfer with PMT insert

Fig. 6 shows wall temperatures for BT and MHTT. Temperatures were given at the top, side and bottom locations for each cross section. The data for the inclination angles of 0°, 90° and −90° were shown. The R245fa mass fluxes and inlet vapor mass qualities x_{in} were about 200 kg/m^2 s and 0.5, respectively. The cooling water

Table 4
The experimental runs and parameters.

Runs	BT or MHTT	θ (°)	P_{in} (kPa)	$T_{r,\,in}$ (°C)	G (kg/m^2 s)	x_{in}	x_{out}	h (kW/m^2 K)	h' (kW/m^2 K)	EF	ΔP_f (kPa)	PEC
1	BT	0	402.1	55.1	199.2	0.498	0.119	1.905	1.882	–	2.70	–
2	MHTT	0	402.9	55.0	199.2	0.505	0.039	2.449	2.380	1.285	7.27	1.090
3	BT	0	410.5	56.0	198.8	0.706	0.236	2.313	2.282	–	3.94	–
4	MHTT	0	409.3	55.8	198.1	0.705	0.127	3.284	3.175	1.420	13.89	1.151
5	BT	0	404.3	55.4	198.5	0.904	0.385	2.714	2.672	–	4.30	–
6	MHTT	0	402.3	55.3	198.1	0.906	0.267	4.150	4.000	1.529	22.25	1.163
7	BT	0	405.9	55.6	296.9	0.404	0.094	2.297	2.268	–	3.69	–
8	MHTT	0	406.0	55.4	298.4	0.397	0.044	3.017	2.919	1.314	15.21	1.038
9	BT	0	406.5	55.8	299.8	0.499	0.161	2.636	2.597	–	3.93	–
10	MHTT	0	406.8	55.5	299.9	0.499	0.102	3.778	3.647	1.434	23.79	1.062
11	BT	0	406.5	55.6	299.8	0.699	0.316	3.233	3.175	–	4.38	–
12	MHTT	0	408.5	55.7	299.6	0.702	0.251	5.148	4.950	1.592	42.64	1.090
13	BT	0	406.9	55.6	398.5	0.304	0.072	2.341	2.305	–	3.98	–
14	MHTT	0	407.3	55.3	398.5	0.304	0.026	3.282	3.174	1.402	20.42	1.068
15	BT	0	405.1	55.5	398.4	0.400	0.138	2.776	2.733	–	4.21	–
16	MHTT	0	405.2	55.1	397.6	0.400	0.093	4.221	4.069	1.521	32.42	1.082
17	BT	0	404.3	55.3	398.8	0.506	0.211	3.234	3.162	–	5.30	–
18	MHTT	0	404.2	55.2	398.5	0.508	0.175	5.329	5.130	1.648	51.04	1.093
19	BT	90	405.1	55.3	199.5	0.502	0.058	2.185	2.164	–	3.05	–
20	MHTT	90	406.5	55.3	199.2	0.500	0.012	3.001	2.916	1.373	16.73	1.034
21	BT	90	405.1	55.4	199.9	0.699	0.208	2.498	2.470	–	3.06	–
22	MHTT	90	406.2	55.4	198.6	0.711	0.108	3.726	3.619	1.492	20.89	1.083
23	BT	90	406.3	55.5	200.1	0.900	0.360	2.848	2.812	–	3.48	–
24	MHTT	90	405.4	55.4	198.2	0.917	0.255	4.473	4.322	1.571	27.51	1.113
25	BT	90	407.1	55.3	299.6	0.391	0.083	2.347	2.317	–	2.83	–
26	MHTT	90	406.7	55.3	300.9	0.388	0.019	3.445	3.339	1.468	21.62	1.046
27	BT	90	407.0	55.4	300.6	0.497	0.164	2.630	2.594	–	3.43	–
28	MHTT	90	408.3	55.5	300.3	0.492	0.082	4.125	3.996	1.569	29.57	1.096
29	BT	90	406.6	55.5	300.2	0.703	0.318	3.225	3.178	–	3.83	–
30	MHTT	90	406.4	55.4	299.0	0.705	0.247	5.243	5.070	1.625	46.38	1.073
31	BT	90	406.5	55.0	400.1	0.298	0.057	2.469	2.439	–	2.80	–
32	MHTT	90	406.8	55.2	400.7	0.298	0.020	3.552	3.463	1.438	29.73	1.033
33	BT	90	403.1	55.1	401.4	0.399	0.140	2.858	2.819	–	3.76	–
34	MHTT	90	404.7	55.1	401.4	0.398	0.091	4.516	4.427	1.580	43.15	1.052
35	BT	90	404.0	55.2	400.9	0.497	0.213	3.343	3.282	–	3.88	–
36	MHTT	90	403.6	55.2	402.0	0.494	0.172	5.661	5.478	1.693	57.79	1.079
37	BT	−90	404.1	55.3	200.2	0.499	0.125	1.728	1.705	–	4.55	–
38	MHTT	−90	404.0	55.2	199.9	0.503	0.022	2.531	2.459	1.465	18.18	1.163
39	BT	−90	402.3	55.2	198.3	0.714	0.265	2.202	2.165	–	4.82	–
40	MHTT	−90	404.4	55.4	199.3	0.719	0.142	3.503	3.388	1.591	21.72	1.238
41	BT	−90	406.6	55.6	200.9	0.900	0.380	2.709	2.662	–	6.30	–
42	MHTT	−90	407.1	55.6	197.3	0.917	0.256	4.298	4.150	1.587	27.69	1.239
43	BT	−90	406.8	55.3	300.2	0.395	0.097	2.131	2.104	–	5.98	–
44	MHTT	−90	406.7	55.3	298.7	0.405	0.044	3.156	3.047	1.481	25.05	1.166
45	BT	−90	406.3	55.4	300.9	0.500	0.177	2.449	2.409	–	6.07	–
46	MHTT	−90	404.4	55.2	299.4	0.508	0.106	3.970	3.834	1.621	32.81	1.224
47	BT	−90	405.2	55.5	302.0	0.696	0.314	3.223	3.161	–	6.82	–
48	MHTT	−90	406.4	54.9	297.2	0.714	0.260	5.349	5.186	1.660	53.83	1.176
49	BT	−90	405.3	55.2	401.5	0.299	0.063	2.329	2.300	–	7.19	–
50	MHTT	−90	405.3	55.0	400.8	0.296	0.025	3.362	3.248	1.444	31.45	1.129
51	BT	−90	407.6	55.6	400.6	0.398	0.134	2.704	2.666	–	7.31	–
52	MHTT	−90	409.5	55.6	399.4	0.400	0.091	4.382	4.226	1.621	43.07	1.206
53	BT	−90	403.5	55.3	400.4	0.499	0.212	3.122	3.072	–	7.83	–
54	MHTT	−90	405.5	55.4	399.9	0.497	0.173	5.445	5.256	1.744	58.93	1.245
55	BT	−90	406.1	55.5	500.7	0.402	0.171	3.204	3.169	–	7.62	–
56	MHTT	−90	405.7	55.5	500.1	0.404	0.149	5.945	5.751	1.854	79.30	1.255

mass flow rates were about 500 kg/h with inlet water temperatures of about 25 °C. Because condensation heat transfer coefficients were different for BT and MHTT, the R245fa outlet vapor mass qualities were different for the two types of tubes. Wall temperatures were higher for MHTT. Thus, PMT decreased temperature difference between R245fa mixture and cooper tube wall, showing decreased condensation thermal resistance and raised condensation heat transfer coefficient. The tube conduction thermal resistances were not changed apparently with and without PMT. Meanwhile, MHTT raised wall temperatures to increase temperature difference between copper tube wall and cooling water. This effect increased heat transfer rate with PMT insert. ΔT_c represents temperature difference between cooling water outlet and inlet in Fig. 6. Eq. (3) shows the heat transfer rate proportional to ΔT_c. The increased heat transfer rates were 19.5%, 17.7% and 13.6% for the three inclination angles, respectively. The enhanced heat transfer rates indicate the total heat transfer coefficient increased by 14–20% with PMT insert. Non-uniform wall temperatures along the tube wall circumference were observed for BT and MHTT at horizontal position due to the buoyancy force effect (see Fig. 6a). Vapor phase tends to populate at the tube top but liquid tends to populate at the tube bottom. Wall temperatures were more uniform for vertical upflow ($\theta = 90°$) and downflow ($\theta = -90°$).

Fig. 7 shows condensation heat transfer coefficients (left column) and enhanced heat transfer factors (right column). Because our experiment kept the same x_{in} for a comparative runs for BT and MHTT, the data were plotted versus x_{in}. The outlet vapor mass qualities (x_{out}) can be found in Table 4. Solid and open symbols

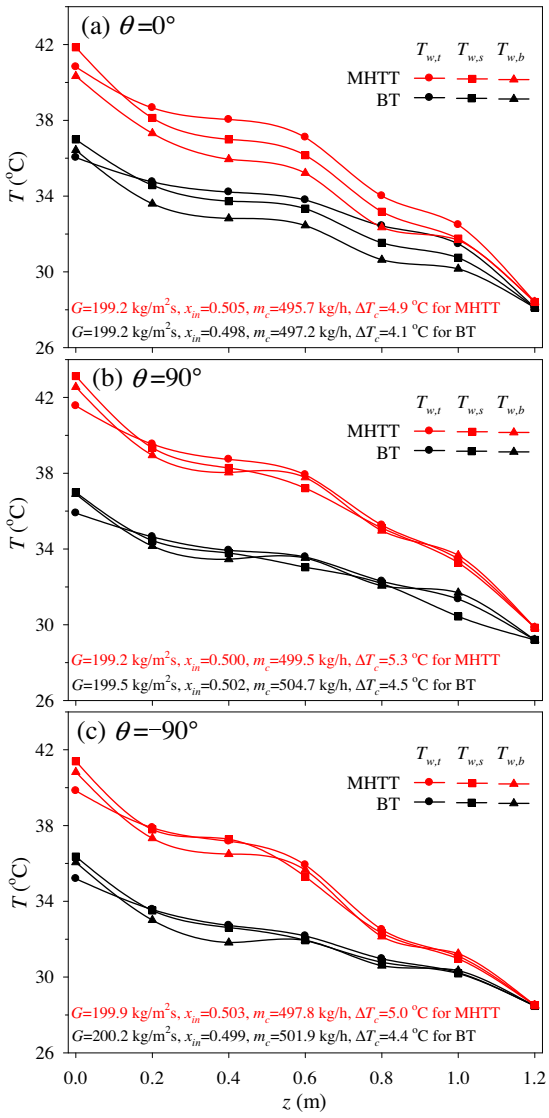

Fig. 6. The modulated condenser tube decreased wall temperatures of the copper tube at three inclination angles.

represented h for MHTT and BT, respectively. MHTT had much larger condensation heat transfer coefficients than BT.

Inclination angles had apparent influence on h for BT and MHTT, especially at low mass fluxes. BT had largest and smallest heat transfer coefficients for vertical upflow ($\theta = 90°$) and vertical downflow ($\theta = -90°$), respectively. The θ dependent h was caused by the flow patterns in the tube. Lips and Meyer [14] investigated convective condensation of R134a in an 8.38 mm inner diameter tube. Their finding shows the strong effect of inclination angles on flow patterns and heat transfer for low mass fluxes and/or vapor mass qualities. The horizontal flow yields stratified flow with thick liquid thickness at the tube bottom. Thus, heat transfer coefficients cannot be the largest among the three inclination angles. The vertical upflow yields the annular flow with strong turbulence on the vapor-liquid interface to have the largest heat transfer coefficients. The vertical downflow yields the annular flow with thick liquid film on the tube wall to have the smallest heat transfer coefficients. The increases of mass flux and/or vapor mass qualities narrowed the difference among the three inclination angles. Our measurements qualitatively matched the observations by Lips and Meyer [14]. MHTT had the largest and smallest h at $\theta = 90°$ and $\theta = 0°$, respectively.

Enhanced heat transfer factor (EF) was defined as the h for MHTT divided by that for BT at the same inclination angle. Covering the present data rage, the EF values are in the range of 1.25–1.85. The EF values are the largest for vertical upflow and smallest for horizontal flow. Both heat transfer coefficients and enhanced heat transfer factors were increased with inlet vapor mass qualities.

Fig. 8 examined heat transfer coefficients and enhanced heat transfer factors versus mass fluxes (G). Mass flux reflects mixture convective component on the heat transfer. The increased mass flux increased the condensation heat transfer coefficient for both BT and MHTT. The h values reached about 6 kW/m^2 K maximally for MHTT. Heat transfer enhancement factors were increased with increases in mass fluxes (see Fig. 8b). Fig. 9 summarized h and EF versus Fr_g, where Fr_g is the Froude number of the vapor phase, which is defined as

$$Fr_g = \frac{G^2 x_{ave}^2}{\rho_f^2 g D_i} \tag{22}$$

where $x_{ave} = 0.5(x_{in} + x_{out})$. The Froude number of vapor phase indicates the inertia force relative to the gravity force. MHTT and BT narrowed the h variance with increases in Fr_g, forming a trapezoid shape distribution. The increase of G and/or x_{ave} raised Fr_g to weaken the inclination angle effect on heat transfer.

Fig. 9b shows the increased EF versus Fr_g. EF at any Fr_g lied in a quadrilateral region with a variance of about 0.2–0.3. Even though both BT and MHTT increased h versus Fr_g and narrowed the difference among the three inclination angles, the flow and heat transfer mechanisms are quite different for BT and MHTT. Therefore, when we plotted the heat transfer enhancement ratio (EF), the EF values are scatted versus Fr_g, even for a same inclination angle.

3.2. The observed flow patterns in the bare tube

Fig. 10 plotted flow pattern maps for $\theta = 0°$, 90° and −90°, respectively. Flow patterns were observed through an empty glass tube having almost the same inner diameter of the copper tube. Flow pattern images were shown in the right column corresponding to the red data point in each subfigure. Stratified-wavy flow (SW) contained settled liquid at the tube bottom and vapor at the tube top, having wavy liquid-vapor interface. Intermittent flow (I) contained wavy vapor-liquid interface, with its tip contacting the tube wall. Churn flow (C) can be regarded as a deformed slug flow. Deformed bubbles are populated in the tube with liquid plugs between two neighboring bubbles. Annular flow (A) contains vapor core and liquid droplets entrained in vapor, leaving a liquid film on the tube wall. Falling film flow (F) happens for the vertical downflow, with vapor core in the tube center and thick liquid film on the tube wall.

At horizontal position ($\theta = 0°$), gravity force is important to influence phase distribution. The SW flow appears in the left-bottom corner, while the A flow happens at large mass fluxes and/or vapor mass qualities. The I flow takes place in-between the SW and A flows (see Fig. 10a). The vertical upflow had C and A flow patterns (see Fig. 10b). The vertical downflow had F and A flow patterns (see Fig. 10c). Transition boundaries among various flow patterns were also marked by the criteria provided in ref. [31] at $\theta = 0°$.

Due to the large tube diameter of 14.81 mm and low surface tension force of R245fa, bubbly flow and slug flow were not observed, but they happened in refs. [32,33]. Froude number, Bond number and Weber number were defined as

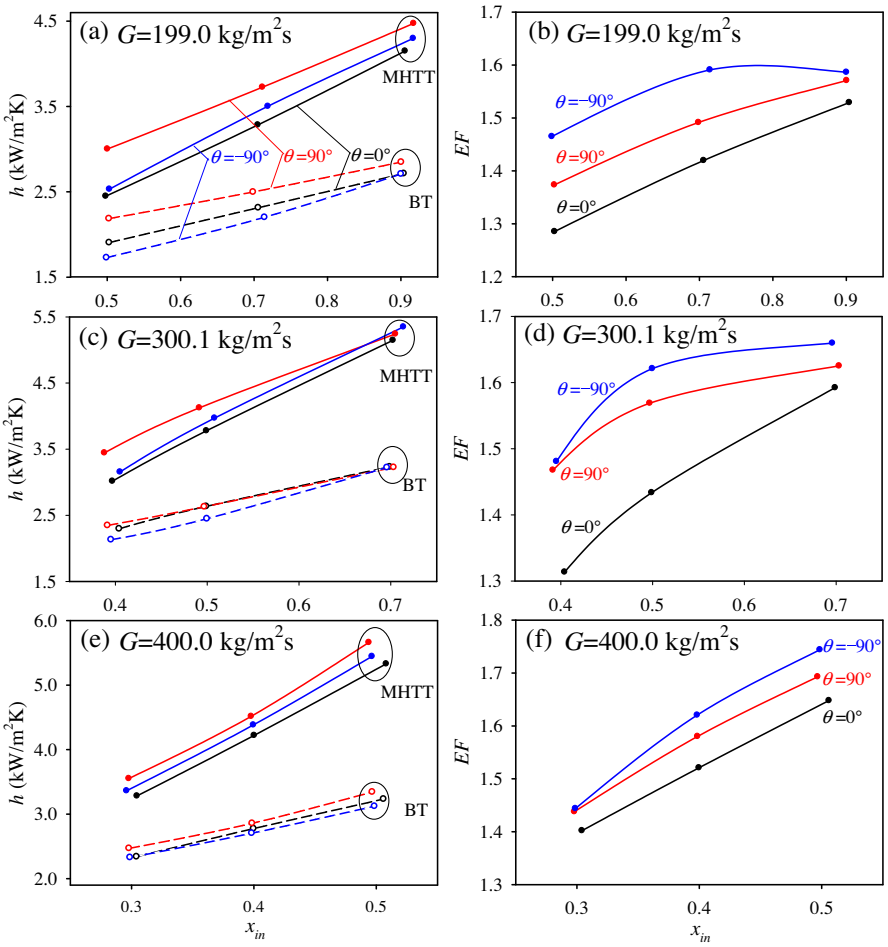

Fig. 7. Condensation heat transfer coefficients and their enhanced heat transfer coefficients at various mass fluxes and inlet vapor mass qualities.

$$Fr = \frac{G^2}{\rho_f^2 g D_i}, \quad Bd = \frac{g(\rho_f - \rho_g)D_i^2}{\sigma}, \quad We = \frac{G^2 D_i}{\rho_f \sigma} \tag{23}$$

where subscripts of f and g represent liquid and vapor phase, respectively, ρ and σ are density and surface tension force, g is the gravity acceleration. Giving the data range, Froude numbers covered a range of 0.166–1.112 to show the importance of both the inertia force and gravity force. Because D_i/σ is large, Bond and Weber numbers had ranges of 258–261 and 44–294, which are significantly larger than one, showing the importance of inertia force and gravity force to suppress surface tension force effect. Bubbly flow and slug flow did not happen because of the large Bond number and Weber number.

3.3. The heat transfer enhancement mechanism

PMT divided tube cross section into a core region and an annular region (see Fig. 2c). It is lyophilic thus only liquid flows towards PMT but vapor phase is prevented from entering PMT. Thus, vapor void fractions near the tube wall are increased. Fig. 11 shows pressure balance. $P_{e,an}$ and $P_{e,co}$ are exit pressures in the annular region and core region, respectively. $P_{u,an}$ and $P_{u,co}$ are upstream pressures in the annular region and core region, respectively. Because fluid streams from annular region and core region are mixed at the tube exit, it is reasonable to assume $P_{e,an} \approx P_{e,co}$. For liquid flow in the core region, $P_{u,co}-P_{e,co}$ includes liquid frictional pressure drop and gravity pressure drop:

$$P_{u,co} - P_{e,co} = \Delta P_{f,co} + \rho_f g L_{ue} \sin(\theta) \tag{24}$$

where L_{ue} is the length between the focus point and the tube exit. For two-phase flow in the annular region, $P_{u,an}-P_{e,an}$ is

$$P_{u,an} - P_{e,an} = \Delta P_{f,an}\phi_{lo}^2 + \rho_m g L_{ue} \sin(\theta) \tag{25}$$

where $\Delta P_{f,an}$ is the frictional pressure drop assuming total two-phase mixture in the annular region flowing as liquid alone, and ϕ_{lo}^2 is the two-phase multiplier having the range of 10–100, ρ_m is the two-phase mixture density in the annular region. Combining Eqs. (24) and (25) and assuming $P_{e,an} \approx P_{e,co}$ yields

$$P_{u,an} - P_{u,co} \approx \Delta P_{f,an}\phi_{lo}^2 - \Delta P_{f,co} + (\rho_m - \rho_f) g L_{ue} \sin(\theta) \tag{26}$$

$P_{u,an}-P_{u,co}$ is the driving force for liquid flow towards PMT, which is the two-phase pressure drop in annular region subtracting the liquid pressure drop in PMT. The two-phase flow theory tells us that it is positive.

3.3.1. Increased h with increase in G and/or x

Two-phase frictional pressure drop is increased with increases in mass fluxes and vapor mass qualities. This increased the driving force for liquid flow from the annular region to the core region, which is the reason for the increased condensation heat transfer coefficients with increases in G and x_{in} (see Figs. 7 and 8).

3.3.2. Condensation heat transfer dependent on inclination angles

The third term of right side of Eq. (26) equals to zero for horizontal flow ($\theta = 0°$). Gravity force has no contribution to the driving force for liquid flow towards the core region. The situation is changed for the vertical downflow ($\theta = -90°$). The term of $(\rho_f-\rho_m)gL_{ue}$ is

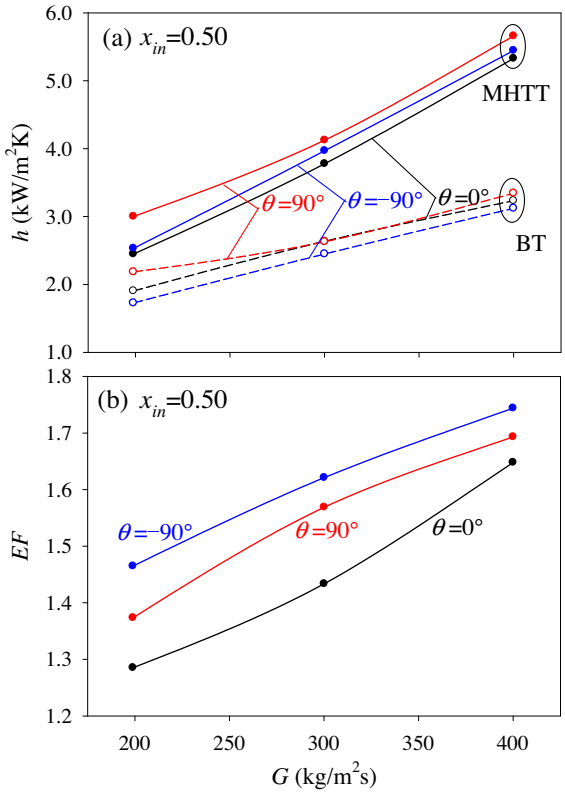

Fig. 8. Effect of mass fluxes on the enhanced condensation heat transfer with PMT insert.

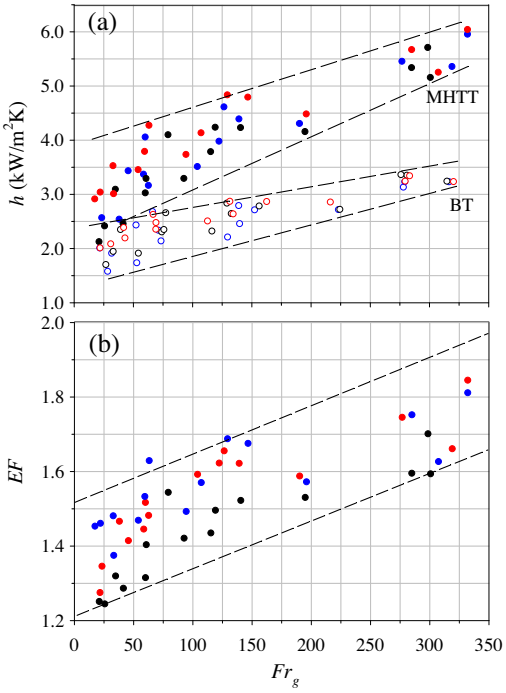

Fig. 9. The summarized condensation heat transfer coefficients and enhanced heat transfer factors with respect to Fr_g (red symbols for $\theta = 90°$, blue symbols for $\theta = -90°$and black symbols for $\theta = 0°$). (For interpretation of the references to colour in this figure legend, the reader is referred to the web version of this article.)

positive and reaches maximum among various inclination angles. The vertical downflow provides the largest driving force for liquid flow from the annular region to the core region, which is helpful for the increment of vapor void fractions near the tube wall to enhance heat transfer. Therefore, MHTT had larger condensation heat transfer coefficients for vertical downflow ($\theta = -90°$) than those for horizontal flow ($\theta = 0°$), see Figs. 7 and 8.

Attention was paid to modulated heat transfer for vertical upflow ($\theta = 90°$). The third term of right side of Eq. (26) is negative to weaken the driving force to capture liquid from the annular region to the core region. It seems that MHTT had the smallest condensation heat transfer coefficients at $\theta = 90°$ among the three inclination angles. However, Figs. 7 and 8 did show the largest heat transfer coefficients at $\theta = 90°$.

Fig. 12a shows two modulated and deformed bubbles in the test section entrance for vertical upflow. The photo was taken through the sight glass tube ahead of the copper tube (see Fig. 2a). Fig. 12b redraws the phase distribution, with white and blue colors representing vapor and liquid phases, respectively. Fig. 12c focused on a deformed bubble. Around the deformed bubble, liquid film on the tube wall flows upwards. At the bubble front, liquid flows from the annular region to PMT. Liquid flows downwards inside PMT. At the bubble tail, liquid flows from PMT inside to annular region. In such a way, liquid circulation around the bubble is established. Thus, liquid mass and momentum exchange across PMT exists. Somewhere far away from the deformed bubble, liquid flows upwards inside PMT. Such flow configuration is consistent with our previous air-water two-phase flow experiment for flow pattern modulations [18].

The phenomenon was caused by the density difference between core region and annular region, in which fluid in the core region is much heavier than that in the annular region. Chen et al. [34] verified the flow structure by multiscale flow simulation. The promoted liquid mass and momentum exchange explains the largest heat transfer coefficients for vertical upflow compared with other flow inclinations.

3.4. Enhanced heat transfer for specific flow patterns

3.4.1. Annular flow modulation

Fig. 13a shows annular flow modulation. In order to verify if PMT is lyophilic to R245fa liquid, we performed liquid capture test by falling R245fa drops on a porous-membrane surface in a pressurized glass chamber. Fig. 13b shows an R245fa droplet spreading on the surface with an initial diameter of 1.48 mm. The drop contacted with the surface at $t = 0$. Then it was quickly spreading and penetrating the pore surface. The wetting area was increased in a circular shape. A wetting diameter of 3.21 mm was formed at $t = 100$ ms. Fig. 13c shows displacement of the wetting area (r) versus time t. The spreading velocity u_r in radial direction is expressed as $u_r = dr/dt$. The spreading velocities are changed from 10.5 mm/s to 6.0 mm/s in a time period of 150 ms.

The PMT lyophilic feature is the basic mechanism for annular flow modulation. Fig. 14 shows comparative flow structures in BT and MHTT, respectively. With PMT insert, liquid drops entrained in vapor were captured by the porous surface and flows towards PMT inside. This significantly decreases the number of drops in vapor near the tube wall. Thus, liquid film on the tube wall becomes thin to enhance condensation heat transfer.

3.4.2. Stratified-wavy flow modulation

The SW flow modulation was observed (see Fig. 15a). The R245fa fluid was used. Cross sections A–A and B–B were in the bare tube section and modulated flow section, respectively (see Fig. 15b). When liquid height is H_l, heat transfer rate is directly related to the tube surface area exposed in vapor:

$$Q_h = \alpha_h \cdot \Delta T \cdot S_v \tag{27}$$

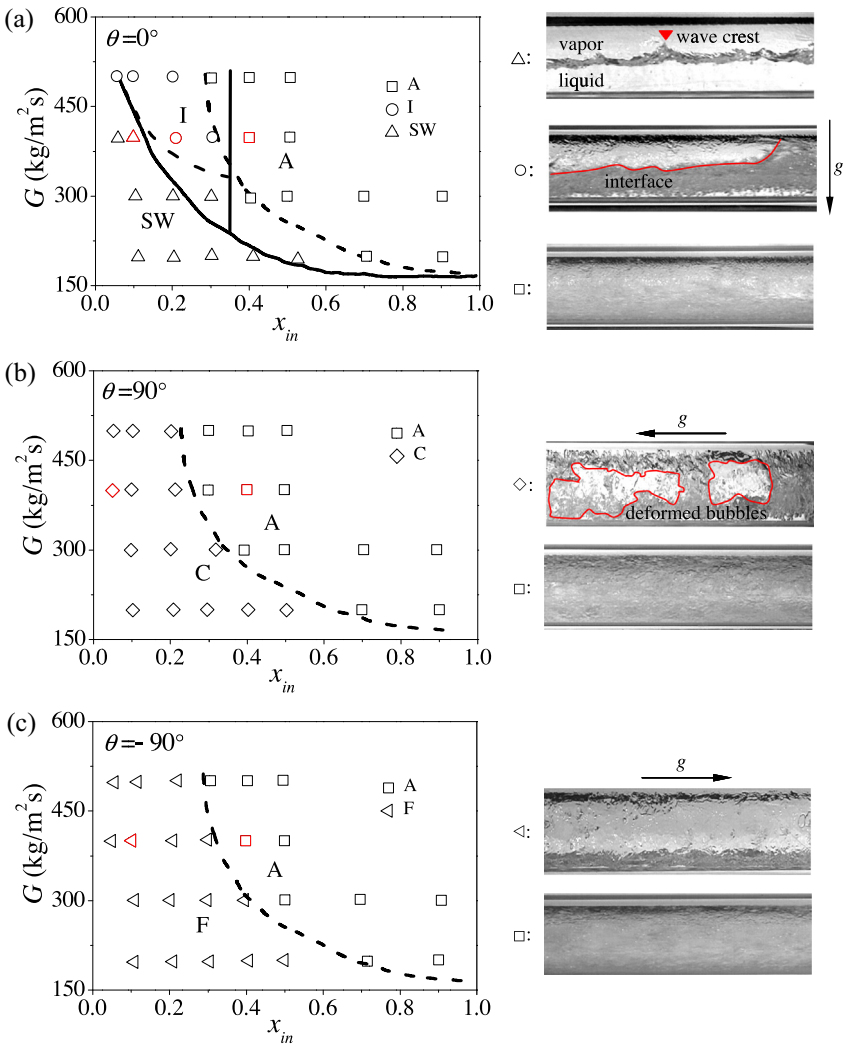

Fig. 10. Flow pattern maps and flow images in the bare tube (the flow direction was from left to right, I: Intermittent flow, SW: stratified-wavy flow, A: annular flow, F: falling film flow, C: churn flow).

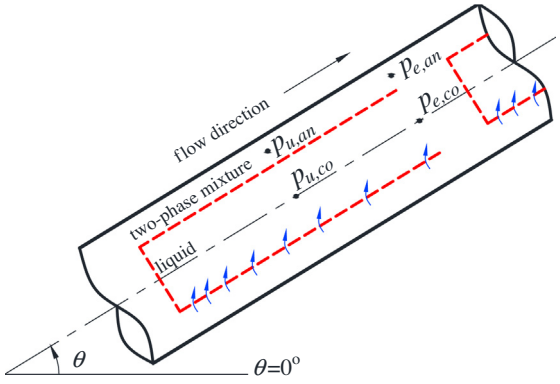

Fig. 11. The pressure balance analysis for MHTT with PMT insert at inclination angle θ.

where Q_h is the heat transfer rate in the tube along a unit flow length, α_h is the thin film condensation heat transfer coefficient, ΔT is the temperature difference between tube wall and saturation temperature. S_v is the circumference length exposed in vapor, which is

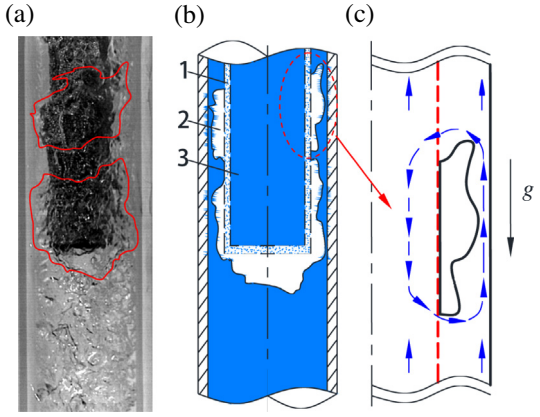

Fig. 12. The promoted liquid mass and momentum exchange across PMT surface (a: the photo of modulated and deformed bubbles for $\theta = 90°$, $G = 199.5$ kg/m^2 s, $x = 0.109$, b: two-dimensional drawing with 1: PMT, 2: modulated and deformed bubble, 3: liquid, c: liquid mass exchange around a modulated and deformed bubble).

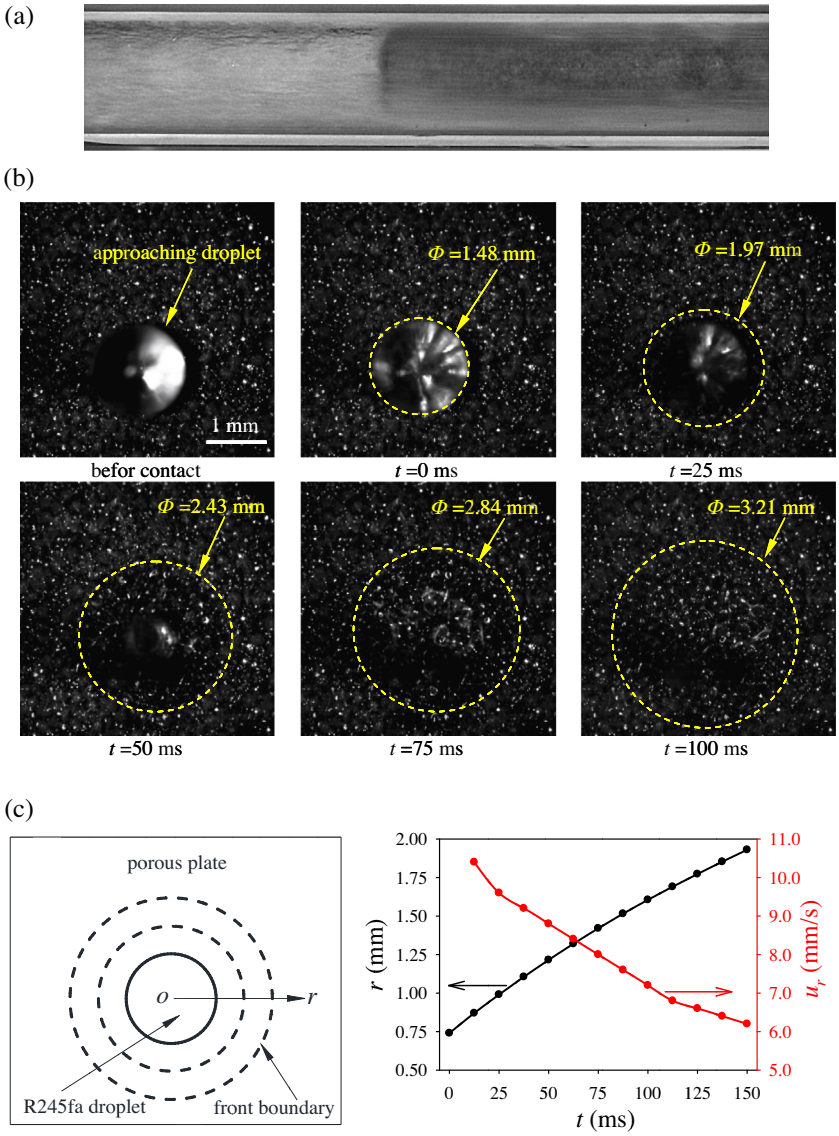

Fig. 13. The porous membrane captured liquid drops ($\theta = 0°$, $G = 398.8$ kg/m^2 s, $x = 0.505$).

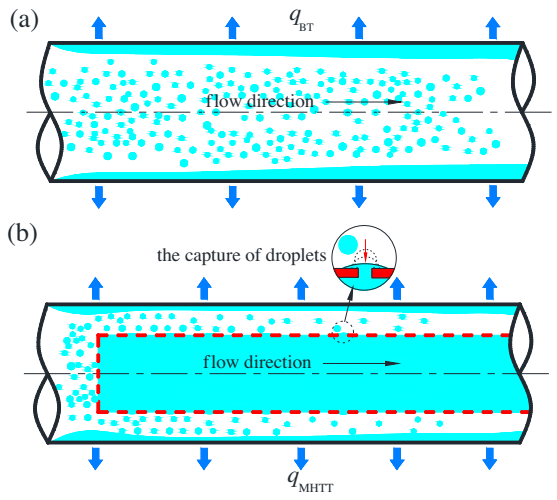

Fig. 14. The annular flow modulation to decrease liquid film thickness on the tube wall.

$$S_v = \begin{cases} D_{gl} \cdot \arccos\left(\frac{2H_l}{D_{gl}} - 1\right) & \text{for } H_l/D_{gl} > 0.5 \\ \pi D_{gl} - D_{gl} \cdot \arccos\left(1 - \frac{2H_l}{D_{gl}}\right) & \text{for } H_l/D_{gl} < 0.5 \end{cases} \quad (28)$$

Comparing the two cross sections in Fig. 15b, heat transfer rate per unit flow length is enhanced by $\tilde{k} = S_{v,B}/S_{v,A}$. Capillary pumping ensured liquid holding within PMT and decreased liquid height in the annular region. Our high speed camera recorded dynamic liquid heights at the tube bottom for BT and MHTT. The image processing procedure is similar to that reported by Ong and Thome [35]. The MATLAB software processed video images to detect liquid-vapor interface and channel wall, which were determined based on the number of image pixels. Fig. 15c shows $H_{l,A}$ and $H_{l,B}$. The average $H_{l,B}$ in MHTT was 0.326, which was significantly lower than $H_{l,A}$ of 0.516. Substituting $H_{l,A}$ and $H_{l,B}$ to Eq. (28) and applying $\tilde{k} = S_{v,B}/S_{v,A}$, $\tilde{k}$ was 1.267. In other words, the PMT inset increased condensation heat transfer rate by 26.7%, well matched the measured 28.5% heat transfer improvement at similar running condition. In summary, the capillary pumping ensured liquid holding in PMT to decrease liquid height in annular region, accounting for the condensation heat transfer enhancement mechanism for stratified flow.

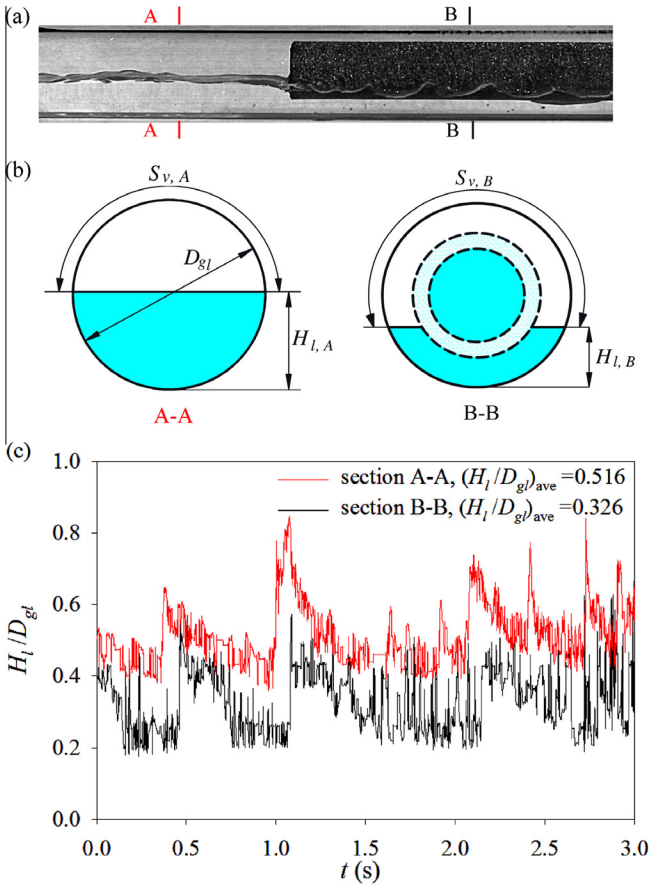

Fig. 15. The stratified flow pattern modulation with $\theta = 0°$, $G = 199.2$ kg/m^2 s, $x = 0.112$.

4. Conclusions

Following conclusions can be drawn:

- MHTT and BT increased condensation heat transfer coefficients with mass fluxes and vapor mass qualities. BT had the largest and smallest heat transfer coefficients for vertical upflow and downflow, respectively. MHTT had the largest and smallest heat transfer coefficients for vertical upflow and horizontal flow, respectively. The enhanced heat transfer factors had a range of 1.25−1.85, which are largest for vertical upflow and smallest for horizontal flow.
- The $h \sim Fr_g$ data points formed a trapezoid region. MHTT and BT narrowed the h variance at larger Fr_g due to the weakened gravity force effect on heat transfer.
- Annular flow, intermittent flow, stratified-wavy flow, churn flow and falling liquid film flow were observed in BT. Bubbly flow and slug flow were not observed due to the large Bond number and Weber number.
- For MHTT, the pressure difference between two-phase flow in annular region and liquid flow in core region drives liquid flow towards the core region. The driving force is increased with increases in G and/or x to enhance the heat transfer enhancement factors.
- For MHTT, the pressure balance analysis explained larger condensation heat transfer coefficients for vertical downflow than horizontal flow. The promoted liquid mass and momentum exchange across the porous membrane yielded the largest condensation heat transfer coefficients for vertical upflow.
- PMT is lyophilic to R245fa liquid. Drops are captured to form liquid flow towards the core region, which is the heat transfer enhancement mechanism for annular flow modulation.
- For stratified flow modulation, the capillary pumping holds liquid in the core region to decrease liquid height in the annular region. Thus, the tube wall surface area exposed by vapor is increased to enhance the heat transfer.

Conflict of interest

None declared.

Acknowledgements

This work was financially supported by the Natural Science Foundation of China (51436004 and 51210011), the National Basic Research Program of China (2011CB710703), and the Fundamental Research Funds for the Central Universities (2014XS50).

References

[1] F.B. Yang, X.R. Dong, H.G. Zhang, Z. Wang, K. Yang, J. Zhang, E.H. Wang, H. Liu, G.Y. Zhao, Performance analysis of waste heat recovery with a dual loop organic rankine cycle (ORC) system for diesel engine under various operating conditions, Energy Convers. Manage. 80 (2014) 243–255.
[2] D. Kaya, M. Eyidogan, F.C. Kilic, Y. Cay, S. Cagman, V. Coban, Energy saving and emission reduction opportunities in mixed-fueled industrial boilers, Environ. Prog. Sustainable Energy 33 (4) (2014) 1350–1356.
[3] W. Han, L. Sun, D. Zheng, H. Jin, S. Ma, X. Jing, New hybrid absorption–compression refrigeration system based on cascade use of mid-temperature waste heat, Appl. Energy 106 (2013) 383–390.
[4] O. Kwon, D. Cha, C. Park, Performance evaluation of a two-stage compression heat pump system for district heating using waste energy, Energy 57 (2013) 375–381.
[5] B.F. Tchanche, G. Lambrinos, A. Frangoudakis, G. Papadakis, Low-grade heat conversion into power using organic Rankine cycles – a review of various applications, Renew. Sustainable Energy Rev. 15 (8) (2011) 3963–3979.
[6] S. Quoilin, M. Van Den Broek, S. Declaye, P. Dewallef, V. Lemort, Techno-economic survey of organic Rankine cycle (ORC) systems, Renew. Sustainable Energy Rev. 22 (2013) 168–186.
[7] M. Imran, B.S. Park, H.J. Kim, D.H. Lee, M. Usman, M. Heo, Thermo-economic optimization of regenerative organic Rankine cycle for waste heat recovery applications, Energy Convers. Manage. 87 (2014) 107–118.
[8] L.H. Zhang, L.J. Wu, Z.A. Lu, Fluid selection for organic Rankine cycle in waste heat power generation during water quenching of blast furnace slag, Ironmak. Steelmak. 40 (2) (2013) 147–152.
[9] E.H. Wang, H.G. Zhang, B.Y. Fan, M.G. Ouyang, Y. Zhao, Q.H. Mu, Study of working fluid selection of organic Rankine cycle (ORC) for engine waste heat recovery, Energy 36 (5) (2011) 3406–3418.
[10] D. Graham, J.C. Chato, T.A. Newell, Heat transfer and pressure drop during condensation of refrigerant 134a in an axially grooved tube, Int. J. Heat Mass Transfer 42 (1998) 1935–1944.
[11] A. Cavallini, D. Del Col, L. Doretti, G.A. Longo, L. Rossetto, Heat transfer and pressure drop during condensation of refrigerants inside horizontal enhanced tubes, Int. J. Refrig. 23 (2000) 4–25.
[12] A. Miyara, Y. Otsubo, Condensation heat transfer of herringbone micro fin tubes, Int. J. Therm. Sci. 41 (2002) 639–645.
[13] S. Laohalertdecha, S. Wongwises, Condensation heat transfer and flow characteristics of R-134a flowing through corrugated tubes, Int. J. Heat Mass Transfer 54 (2011) 2673–2682.
[14] S. Lips, J.P. Meyer, Experimental study of convective condensation in an inclined smooth tube. Part I: inclination effect on flow pattern and heat transfer coefficient, Int. J. Heat Mass Transfer 55 (2012) 395–404.
[15] A. Cavallini, S. Bortolin, D. Del Col, M. Matkovic, L. Rossetto, Condensation heat transfer and pressure losses of high and low pressure refrigerants flowing in a single circular minichannel, Heat Transfer Eng. 32 (2) (2011) 90–98.
[16] R. Gupta, D.F. Fletcher, B.S. Haynes, Taylor flow in microchannels: a review of experimental and computational work, J. Comput. Multiphase Flows 2 (2010) 1–32.
[17] H.X. Chen, J.L. Xu, Z.J. Li, F. Xing, J. Xie, W. Wang, W. Zhang, Flow pattern modulation in a horizontal tube by the passive phase separation concept, Int. J. Multiphase Flow 45 (2012) 12–23.
[18] H.X. Chen, J.L. Xu, J. Xie, F. Xing, Z.J. Li, Modulated flow patterns for vertical upflow by the phase separation concept, Exp. Therm. Fluid Sci. 52 (2014) 297–307.
[19] D.L. Sun, J.L. Xu, Q.C. Chen, Z. Cao, Numerical study of flow pattern modulation in a vertical phase separation condenser tube, Chin. Sci. Bull. 58 (13) (2013) 1592–1598.

[20] Y.R. Lee, C.R. Kuo, C.H. Liu, B.R. Fu, J.C. Hsieh, C.C. Wang, Dynamic response of a 50 kW organic Rankine cycle system in association with evaporators, Energies 7 (4) (2014) 2436–2448.
[21] Z. Cao, J.L. Xu, D.L. Sun, J. Xie, F. Xing, Q.C. Chen, X.D. Wang, Numerical simulation of modulated heat transfer tube in laminar flow regime, Int. J. Therm. Sci. 75 (2014) 171–183.
[22] J.P. Holman, W.J. Gajda, Experimental Methods for Engineers, fourth ed., McGraw-Hill, New York, 1994.
[23] C. Tropea, A.L. Yarin, J.F. Foss, Springer Handbook of Experimental Fluid Mechanics, vol. 1, Springer Science & Business Media, 2007.
[24] F.W. Dittus, L.M.K. Boelter, Heat transfer in automobile radiators of the tubular type, Int. Commun. Heat Mass Transfer 12 (1) (1985) 3–22.
[25] M.M. Shah, A general correlation for heat transfer during film condensation inside pipes, Int. J. Heat Mass Transfer 22 (4) (1979) 547–556.
[26] M.H. Kim, J.S. Shin, Condensation heat transfer of R22 and R410A in horizontal smooth and microfin tubes, Int. J. Refrig. 28 (6) (2005) 949–957.
[27] S. Lips, J.P. Meyer, Experimental study of convective condensation in an inclined smooth tube. Part II: inclination effect on pressure drops and void fractions, Int. J. Heat Mass Transfer 55 (1) (2012) 405–412.
[28] D. Chisholm, Pressure gradients due to friction during the flow of evaporating two-phase mixtures in smooth tubes and channels, Int. J. Heat Mass Transfer 16 (2) (1973) 347–358.
[29] X.Y. Zhang, Z.C. Liu, W. Liu, Numerical studies on heat transfer and flow characteristics for laminar flow in a tube with multiple regularly spaced twisted tapes, Int. J. Therm. Sci. 58 (2012) 157–167.
[30] J.F. Fan, W.K. Ding, J.F. Zhang, Y.L. He, W.Q. Tao, A performance evaluation plot of enhanced heat transfer techniques, Int. J. Heat Mass Transfer 52 (2009) 33–44.
[31] J.E. Hajal, J.R. Thome, A. Cavallini, Condensation in horizontal tubes, Part 1: two-phase flow pattern map, Int. J. Heat Mass Transfer 46 (18) (2003) 3349–3363.
[32] M.K. Dobson, Heat transfer and flow regimes during condensation in horizontal tubes, Air Conditioning and Refrigeration Center, ACRC, College of Engineering, University of Illinois at Urbana-Champaign, 1994.
[33] J.W. Coleman, S. Garimella, Two-phase flow regimes in round, square and rectangular tubes during condensation of refrigerant R134a, Int. J. Refrig. 26 (2003) 117–128.
[34] Q.C. Chen, J.L. Xu, D.L. Sun, Z. Cao, J. Xie, F. Xing, Numerical simulation of the modulated flow pattern for vertical upflows by the phase separation concept, Int. J. Multiphase Flow 56 (2013) 105–118.
[35] C.L. Ong, J.R. Thome, Macro-to-microchannel transition in two-phase flow: Part 1–two-phase flow patterns and film thickness measurements, Exp. Therm. Fluid Sci. 35 (2011) 37–47.